

Journal of Materials Chemistry A

Materials for energy and sustainability

Accepted Manuscript

This article can be cited before page numbers have been issued, to do this please use: M. Mooste, J. Müller-Hülstede, J. Buschermöhle, K. Ruecker, T. Zierdt, J. Ewert, K. Fuhrmann, N. Harder, M. Wilhelm, P. Wagner, D. Schonvogel and K. A. Friedrich, *J. Mater. Chem. A*, 2026, DOI: 10.1039/D6TA01012A.



This is an Accepted Manuscript, which has been through the Royal Society of Chemistry peer review process and has been accepted for publication.

Accepted Manuscripts are published online shortly after acceptance, before technical editing, formatting and proof reading. Using this free service, authors can make their results available to the community, in citable form, before we publish the edited article. We will replace this Accepted Manuscript with the edited and formatted Advance Article as soon as it is available.

You can find more information about Accepted Manuscripts in the [Information for Authors](#).

Please note that technical editing may introduce minor changes to the text and/or graphics, which may alter content. The journal's standard [Terms & Conditions](#) and the [Ethical guidelines](#) still apply. In no event shall the Royal Society of Chemistry be held responsible for any errors or omissions in this Accepted Manuscript or any consequences arising from the use of any information it contains.

Fe, Co, and ZIF-8 co-doped catalysts with carbon nanotube and SiOC composite backbone for high-temperature PEM fuel cell cathode

Marek Mooste,^{a,b*} Julia Müller-Hülstede,^a Julia G. Buschermöhle,^a Konstantin K. Rücker,^a Tanja Zierdt,^a Jana Ewert,^a Killian Fuhrmann,^a Nils Harder,^a Michaela Wilhelm,^c Peter Wagner,^a Dana Schonvogel,^a K. Andreas Friedrich^d

^a*Institute of Engineering Thermodynamics, German Aerospace Center (DLR), Carl-von-Ossietzky-Str. 15, 26129 Oldenburg, Germany.*

^b*Institute of Chemistry, University of Tartu, Ravila 14a, 50411 Tartu, Estonia.*

^c*Advanced Ceramics, University of Bremen, Am Biologischen Garten 2, IW3, 28359 Bremen, Germany*

^d*Institute of Engineering Thermodynamics, German Aerospace Center (DLR), Pfaffenwaldring 38-40, 70569, Stuttgart, Germany*

Abstract

The development of high-temperature proton exchange membrane fuel cell (HT-PEMFC) technology is crucial for implementing the hydrogen economy and decarbonising (heavy) transport and aviation sectors. To replace the Pt-based materials at the HT-PEMFC cathode, we propose a Fe, Co, and N-functionalised catalyst with a nanocarbon backbone consisting of carbon nanotube (CNT) and silicon oxycarbide (SiOC) blend. The CoFe-N-CNT/PDC catalyst is prepared using the Zeolitic imidazolate framework-8 (ZIF-8) as a nitrogen source via pyrolysis, followed by an acid-leaching step. Preliminary testing of oxygen reduction reaction (ORR) activity was conducted comparatively using a rotating ring-disc electrode (RRDE) method at room temperature in 0.5 M H₃PO₄ and with a high-temperature gas diffusion electrode (HT-GDE) half-cell setup at 160 °C in conc. H₃PO₄. Comparative stability testing under RRDE and HT-GDE conditions showed the superior durability of PDC in the catalyst backbone. In more detail, the voltage loss of 36 mV was observed after a 3-hour HT-GDE test at a constant 100 mA cm⁻² for CoFe-N-PDC catalyst, while Fe-N-C (Pajarito Powder, LLC) showed the corresponding value of 80 mV. The maximum power density (P_{\max}) with CoFe-N-CNT/PDC in HT-GDE of 187 mW cm⁻² was obtained, outperforming the P_{\max} of 153 mW cm⁻²

*Corresponding author. Tel +372 737 5177; E-mail address: marek.mooste@ut.ee



² for Fe-N-C. During the HT-PEMFC single-cell tests, the Fe-N-C with P_{\max} of 134 mW cm⁻² surpassed the CoFe-N-CNT/PDC and CoFe-N-CNT cathodes (P_{\max} of 112-124 mW cm⁻²). The high activity towards the ORR of the CoFe-N-CNT/PDC was attributed to the presence of Fe-, Co-, and N-based active sites, as well as an optimised nanocarbon backbone.

Keywords: electrocatalysis, oxygen reduction reaction, non-precious metal catalyst, high-temperature PEMFC, dual-atom catalysts, ZIF-8

1. Introduction

The development of hydrogen technologies is necessary for a clean, sustainable energy economy. It is important to deploy renewable hydrogen in areas with the greatest potential for decarbonisation, making hydrogen an ideal solution for (heavy) transportation.¹ The low-temperature proton exchange membrane fuel cell (LT-PEMFC) is a clean-energy conversion device that is already used in the automotive industry for light-duty vehicles (LDVs).² An attractive alternative to LT-PEMFC is the high-temperature proton exchange membrane fuel cell (HT-PEMFC), which is better suited for heavy-duty vehicles (HDVs) and the aviation sector.³⁻⁶ The advantages of HT-PEMFCs include, e.g., the absence of liquid water, easier thermal management, a perfluoroalkyl and polyfluoroalkyl substances (PFAS)-free phosphoric-acid-doped polybenzimidazole (PA-PBI) membrane, high resistance to CO impurities, and the possibility to use syngas as fuel.⁷⁻¹⁰

Currently, Pt-based nanocarbon (Pt/C) materials are used for oxygen reduction reaction (ORR) electrocatalysis at the cathodes of LT- and HT-PEMFC, which hinders the widespread use of these devices. The main Pt/C-specific problems in HT-PEMFC are the high cost and scarcity of Pt, lower durability compared to LT-PEMFC, and Pt poisoning by phosphate anions from the PA-PBI membrane, necessitating impractically high catalyst loadings.^{6, 11-13} As one possible approach to mitigate the poisoning problem of Pt and to increase the activity towards



the ORR in HT-PEMFC conditions, the incorporation of transition metal (TM, e.g., Co, Ti, Fe) compounds with the Pt/C catalysts has been successfully performed in several studies.¹⁴⁻¹⁶ Furthermore, to completely avoid the use of platinum-group-metal (PGM)-based catalysts at the HT-PEMFC cathode, the development of transition metal-nitrogen-carbon (M-N-C) materials has attracted increased attention.¹⁷⁻¹⁹

The primary issues of M-N-C in acidic HT-PEMFC conditions are demetallation, nitrogen protonation, and carbon oxidation, all of which contribute to poor long-term durability as ORR electrocatalysts at the cathode.^{20, 21} Durability becomes particularly important for HDV applications due to the extended driving lifetime.² The most studied non-PGM materials for HT-PEMFC cathode are currently Fe-N-C, whose durability issues are caused by oxidation of carbon in an acidic environment and the demetallation of nitrogen-coordinated iron (Fe-N_x) active sites for ORR by O₂ itself. Additionally, both processes are facilitated by reactive oxygen species (ROS), which form due to the presence of Fe²⁺ catalysing the Fenton reaction.²² Therefore, scavenging ROS or M-N-C modification to prevent ROS formation is needed, e.g., via incorporating additional TM into the Fe-N-C composition.^{23, 24} The construction of bimetallic M-N-C (e.g., Fe/Co, Fe/Mn, and Fe/Cu) materials can effectively improve the catalyst's stability and activity towards the ORR.²⁵⁻²⁷ These M-N-C materials contain bimetallic sites that exhibit a synergistic effect, which facilitates ORR kinetics by significantly increasing the binding energy of ORR intermediates and lowering the ORR activation energy barrier.^{21, 28}

Among bimetallic M-N-C, the Fe and Co combination is known to provide increased stability for the ORR catalysts in acidic conditions as strong interaction between Fe-N_x and Co-N_x could stabilise the catalyst against migration and agglomeration.^{29, 30} Also, the Fe-N_x, Co-N_x and Fe/Co-N_x are known to exhibit high electrocatalytic activity towards the ORR.³¹⁻³⁴ For example, different CoFe-N-C cathode equipped anion exchange membrane fuel cell (AEMFC)



tests have shown very good performance with the peak power density (P_{\max}) of 0.5–1.0 W cm⁻².^{35–37} Also, Fe and Co combination was found to be optimal for the HT-PEMFC cathode in a recent investigation, where Fe/Co, Fe/Cu, and Fe/Mn bimetallic M-N-C were compared.³⁸

The development of extremely robust catalytic supports suitable for the harsh HT-PEMFC environment is very important.¹⁸ In numerous studies, the polymer-derived carbon (PDC) subclass silicon oxycarbide (SiOC) has been shown to be suitable as a M-N-C support material due to its high chemical and thermal stability, e.g., for AEMFC and zinc-air battery (ZAB).^{39–42} For the HT-PEMFC cathode application, the relatively low specific surface area (SSA) of SiOC was found as one shortcoming limiting the high density of active sites for ORR.^{38, 43}

Multi-walled carbon nanotubes (CNT) meet the stability criteria for HT-PEMFC conditions, exhibit high corrosion resistance, and could also increase the SSA.^{44, 45} Therefore, combining CNT and PDC into the M-N-C backbone could yield a composite nanocarbon that is suitable for the HT-PEMFC cathode.

In the present investigation, various binary TM and N co-doped PDC/CNT composite M-N-C materials were prepared for the HT-PEMFC cathode. Zeolitic imidazolate framework-8 (ZIF-8) from the previous investigation was used as the N-source.³⁸ The preliminary electrocatalyst ORR activity evaluation was performed comparatively in two systems: a rotating ring-disc electrode (RRDE) at room temperature (RT) and a high-temperature gas diffusion electrode (HT-GDE) half-cell setup tests at 160 °C. Based on the HT-GDE results, which testing conditions most closely match the target application, the Co- and Fe-containing N-doped PDC/CNT and CNT catalysts were ultimately employed at the HT-PEMFC cathode with a commercial Fe-N-C (Pajarito Powder, LLC) as a comparison.



2. Experimental

2.1. Catalyst material synthesis

The nanocarbon supports used in the present investigation were CNT (multi-walled carbon nanotubes 95%, OD: 10-30 nm, L: 5-15 μm , CP-0006-SG, IoLiTec Ionic Liquids Technologies GmbH) and SiOC-based PDC developed in previous work.^{38, 39} The preparation route of PDC is given in Section S1 of the Supporting Information. Specific nanocarbons or their 1:1 blend were mixed with ZIF-8 (Basolite® Z1200, Sigma-Aldrich) and TM salts in methanol (99.9%, Thermo Scientific Chemicals) by ultrasonication for 2 hours followed by evaporating the solvent at 60 °C in an oven. The TM salts used in various combinations were iron(II) acetylacetonate (FeAcac, 95%, abcr GmbH), manganese(II) acetylacetonate (MnAcac, Sigma Aldrich), and cobalt(II) acetylacetonate (CoAcac, Sigma Aldrich). The specific amounts (wt%) of used precursors and the final catalyst designations are given in Table S1. The pyrolysis of the dried mixture was performed in N₂ environment at 950 °C with a dwelling time of 1 h according to the previously optimised procedure.³⁸ Similarly, the 16-hour acid leaching procedure at 90 °C in 2 M H₂SO₄ (96%, Merck)^{46, 47} was applied to all of the prepared catalysts, which was previously found to be beneficial for HT-PEMFC cathodes of M-N-C type.³⁸ The acid leaching was performed with ca 50 mg of catalyst in ca 50 ml of acid solution on a stovetop with a magnetic stirrer (400 rpm) and using a condenser. After leaching, the catalyst was filtered with a polyethersulfone filter (pore size 0.22 μm) by washing with MilliQ water until pH = 7 was obtained, dried at 60 °C, and subjected to second pyrolysis in the very same conditions as the first pyrolysis. The outline of the preparation route for the CoFe-N-CNT/PDC catalyst material is depicted in Scheme S1.



2.2. Physical characterisation

View Article Online
DOI: 10.1039/D6TA01012A

Scanning electron microscopy with energy-dispersive X-ray spectroscopy (SEM-EDS) analyses were carried out on gold-sputtered (48 seconds) M-N-C powders prepared with the sputtering machine Sputter Coater 108 Auto (Cressington). The SEM experiments were conducted with SUPRA 40 (Zeiss) equipped with SE2 detector for the images, and the XFlash 6|30 (Bruker) detector for the EDS. Nitrogen adsorption-desorption experiments at 77 K were performed using a Belsorp-Mini (Bel Japan Inc.) to determine the SSA via the Brunauer-Emmett-Teller (BET) method. M-N-C powders (particle size < 300 μm) were pre-conditioned under vacuum at 200 $^{\circ}\text{C}$ for 24 h prior to the measurements.

Raman spectroscopy measurements were performed using a Horiba LabRAM Aramis. A 532 nm laser with a power of 5 mW, a 300 gr mm^{-1} grating, and an objective with 50 \times magnification was used. The data were collected with 120 acquisitions at an integration time of 2 s. The X-ray diffraction (XRD) analysis was performed using a Bruker D8 Advance diffractometer with a Ni-filtered Cu $K\alpha$ radiation source and a LynxEye line detector. The diffraction patterns were collected with a 0.013 $^{\circ}$ 2θ step from 5 $^{\circ}$ to 89 $^{\circ}$, with a counting time of 534 s per step. The description of inductively coupled plasma mass spectrometry (ICP-MS) measurements is provided in Section S2.

High-resolution transmission electron microscopy (HR-TEM) data were collected with Jeol 2100F S-TEM device (magnification: 50 \times -1,500,000 \times , acceleration voltage: 80 kV - 200 kV). EDS measurements were performed with an Oxford AZTEC EDX-System with an SDD detector (X-Max80, 80 mm^2 detector area, resolution 129 eV (Mn K), 1 million counts per sample). The samples for HR-TEM and EDS were prepared by suspending 2-5 mg of M-N-C powder in 5 mL of ethanol and sonicated for 30 minutes. 2 \times 5 μL of suspension was dropped on a TEM grid and dried in air at RT.



For X-ray Photoelectron Spectroscopy (XPS) analyses, an ESCALAB 250Xi (Thermo Fisher) with monochromatic Al-K α radiation and a beam diameter of 650 μm was used. For the survey spectra, three scans were recorded using a transit energy of 100 eV, a dwell time of 20 ms, and a step size of 1 eV. High-resolution XP-spectra for the elements C (1s, 3 scans), O (1s, 5 scans), N (1s, 10 scans), Si (2p, 10 scans), Fe (2p, 15 scans), Co (2p, 15 scans) and Zn (2p, 3 scans) were recorded with a transit energy of 20 eV, a dwell time of 50 ms and a step size of 0.02 eV. For Peak fitting, the software AvantageTM V6 (Thermo Fisher) was used, utilising a smart background and a Gauss-Lorentz line shape.

2.3. RRDE and HT-GDE half-cell studies

The specific details for ORR studies with RRDE method at RT and HT-GDE half-cell setup tests at 160 $^{\circ}\text{C}$ are given in Section S3.

2.4. HT-PEMFC testing

HT-PEMFC single cell test station from Schubert GmbH equipped with a quickCONNECT fixture (qCF 5/100 HT, balticFuelCells) was employed. The fabrication route for the membrane electrode assembly (MEA) and HT-PEMFC test protocols were adapted from recent investigations.^{38, 48} Three cathode catalysts (Fe-N-C (PMF-011904, Pajarito Powder, LLC), CoFe-N-CNT/PDC, and CoFe-N-CNT) were investigated using the same gas diffusion layer (GDL), ink composition, and drop casting technique as used for the HT-GDE tests (Section S3) with a final M-N-C loading of $3.5 \pm 0.1 \text{ mg cm}^{-2}$ (confirmed by ICP-MS). The cathode, PA-PBI membrane (Celtec[®]-P, BASF, pre-soaked in 50% H₃PO₄ for 24 h), and commercial Celtec[®]-based Pt/C anode ($0.86 \text{ mg}_{\text{Pt}} \text{ cm}^{-2}$) were sandwiched by hot pressing (1.0 kN for 30 s at 140 $^{\circ}\text{C}$) using TRG 2 pneumatic lab presses (Paul-Otto Weber GmbH) into the 4.05 cm² MEA outlined with Kapton[®] frames. Prior to pressing, the thickness of every MEA



component was measured with a digital thickness dial gauge (Käfer Messuhrenfabrik GmbH & Co. KG), and the stainless-steel shim shields with 80 % of the total thickness of all MEA components were used to prevent over-crushing of the MEA. The pressing was followed by thermal annealing in air at 160 °C for 30 min in an FD 53 drying and heating oven with forced convection (BINDER GmbH). The MEA performance was evaluated with a cell compression of 0.75 MPa in a cell fixture cF5/100 HT Gr V1.4 with serpentine graphitic flow fields (balticFuelCells). After the gas tightness test with N₂, the gases were switched to dry H₂/O₂ (stoichiometry 1.5/9.5) at a constant load of 100 mA cm⁻². After reaching 160 °C, a galvanostatic polarisation curve was recorded. Next, an external potentiostat, Modulab2100A (Ametek), equipped with a booster (12 V/20 A), was connected to the cell for electrochemical impedance spectroscopy (EIS) and cyclic voltammetry (CV). EIS was recorded in a frequency range of 100 kHz to 100 mHz at a fixed current density of 0.1 A cm⁻² with an amplitude of 10 mV r.m.s. and an equilibration time of 5 min. The CV testing was performed at the N₂ flow rate of 0.1 L min⁻¹ at the cathode and a H₂ flow rate of 0.1 L min⁻¹ at the anode.

3. Results and discussion

3.1. Physical characterisation of the catalysts

As one of the main aims of this paper was the investigation of the nanocarbon (composite) backbone influence on the ORR activity of the CoFe-N-C catalyst, then corresponding materials with various nanocarbon structures and their precursors were subjected to physical characterisation. The Raman spectrum of the pristine CNT exhibits the characteristic peaks of D (1335 cm⁻¹), G (1565 cm⁻¹), and D2 (2670 cm⁻¹) inherent to the spectra of multi-walled carbon nanotubes (Fig. 1a).^{49, 50} The G band corresponds to the graphite (common to all sp² systems), D conforms to structural defects or contaminants, and 2D to second-order Raman scattering process, which is known as an overtone of the D mode. The degree of graphitization



(I_D/I_G ratio) indicates that the pristine CNTs are already rather defective, and pyrolysis with ZIF-8, metal precursors, and PDC does not significantly affect the already highly defective carbon structure according to Raman spectroscopy data. In the case of precursor CNT-free material, CoFe-N-PDC, the Raman signals (D, G, and 2D) very likely originate from the carbon structure formed during the pyrolysis of ZIF-8 and TM acetylacetonates as these peaks are absent in the pristine PDC. This is also supported by the visibly broader G band and the weaker 2D band, which are characteristic of functionalised materials and amorphous carbon.⁵¹ Furthermore, the Raman spectrum of CoFe-N-PDC is also very similar to the ones of binary TM containing PDC catalysts functionalised with N using dicyandiamide (DCDA) in our parallel investigation for ZAB application.³⁹ This indicates that the carbon formed during the pyrolysis of ZIF-8 and DCDA with TM species could exhibit a similar structure, e.g., the formation of CNTs is well documented for both N sources.^{39, 52-54}

N_2 adsorption-desorption studies (Fig. 1b, Table 1) show that the inclusion of CNT could be beneficial for increasing the SSA of the catalyst, as the difference in BET surface area (S_{BET}) between PDC and CNT precursors is 10×. Concurrently, the S_{BET} value for both CoFe-N-C materials with PDC and CNT/PDC backbone is very similar, ca 177 m² g⁻¹, while only in the case of CoFe-N-CNT, the highest S_{BET} of ca 200 m² g⁻¹ is obtained. This indicates that the pyrolysis of ZIF-8 with TMs creates additional nanocarbon material (e.g. CNTs)^{38, 40} with considerable contribution to the overall SSA. Both CNT-containing CoFe-N-C samples exhibit type IV isotherms with a hysteresis loop, indicating micro-mesoporous materials. The mesopores are necessary to ensure the mass transport of O₂ molecules and electrolyte access, while micropores could provide a high density of ORR active sites.^{55, 56} Moreover, the lower d_p value for all CoFe-N-C compared to the precursor materials refers to the micropore formation due to the evaporation of Zn during pyrolysis as known for ZIF-8 containing catalysts.⁵⁷



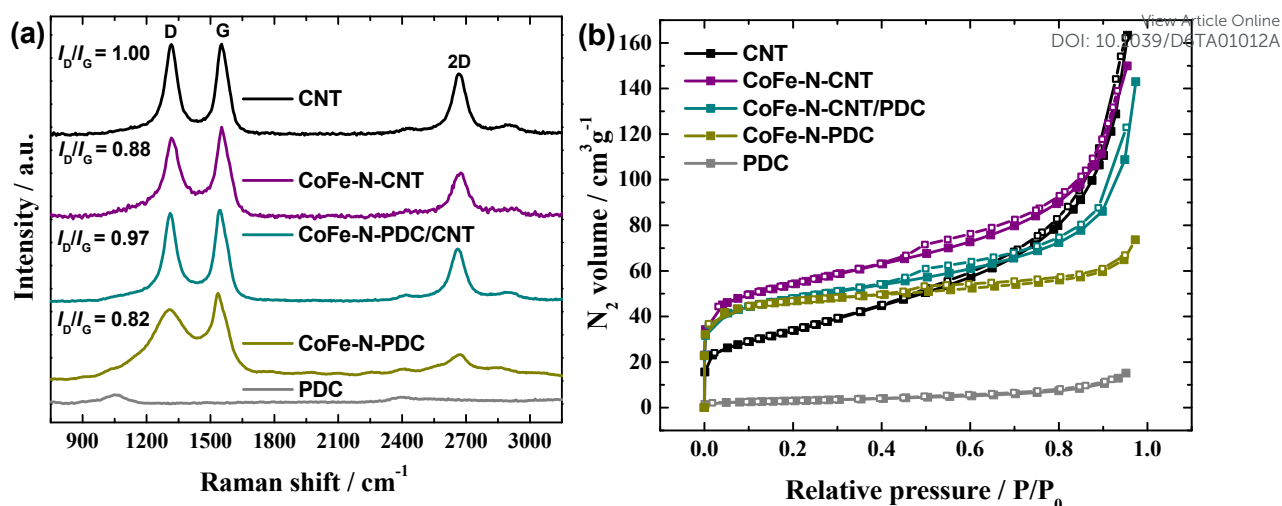


Fig. 1 (a) Raman spectra and (b) N₂ adsorption-desorption isotherms for different catalyst materials. (■) Adsorption and (□) desorption measurement points.

Table 1 Textural properties for different catalyst materials shown in Fig. 1b, monolayer volume (V_m), BET surface area (S_{BET}), total pore volume (V_{tot}) and mean pore diameter (d_p).

	PDC	CNT	CoFe-N-CNT	CoFe-N-CNT/PDC	CoFe-N-PDC
$V_m / \text{cm}^3 \text{g}^{-1}$	2.45	27.7	45.8	40.6	40.8
$S_{\text{BET}} / \text{m}^2 \text{g}^{-1}$	10.67	120.5	199.1	176.6	177.5
$V_{\text{tot}} / \text{cm}^3 \text{g}^{-1}$	0.023	0.252	0.232	0.221	0.114
d_p / nm	8.77	8.39	4.66	5.01	2.57

Altogether, all CoFe-N-C materials prepared herein could host a higher number of active sites for ORR according to the S_{BET} value compared to the CoFe-N-SiOC ($S_{\text{BET}} = 132 \text{ m}^2 \text{g}^{-1}$) from previous work³⁸ indicating to the more promising ORR catalyst design.

The XRD patterns in Fig. 2a and b are divided into PDC- and CNT-containing materials, respectively, along with the specific backbone precursors, to better understand the influence of the carbon composite components. Firstly, the graphite (IMERYL Graphite & Carbon) powder in the PDC composition yields a very intense XRD reflex (Fig. S1), which suppresses all less intense reflexes similarly to the previous investigation.³⁸ Therefore, the carbon reflexes at 26-26.5° in Fig. 2 are shown out of scale. In the case of all CoFe-N-C materials, the reflex for FeCo alloy is registered with the strongest reflex at ca 45° similarly to the previous investigations of different M-N-C catalysts with the Fe and Co combination.^{38, 58, 59} In the case



of CNT and CNT-based catalysts (Fig. 2b), the XRD reflexes of molybdenum carbide (Mo_2C) are observed, which are very likely the residue from the preparation of CNT (CP-0006-SG, IoLiTec) by the chemical vapour deposition method.

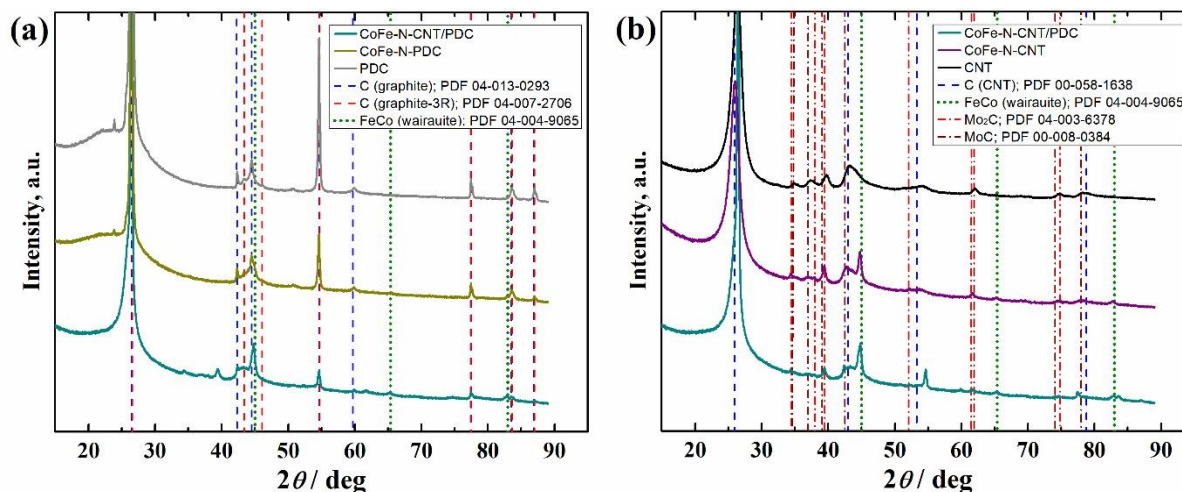


Fig. 2 XRD patterns for different catalyst materials and their backbone precursors for (a) PDC-, (b) CNT-containing materials.

The SEM and TEM images of the CoFe-N-C catalysts (Fig. 3) revealed the morphology of the various nanocarbon composite backbones. The CNTs are observed in the case of all catalyst materials, whereas in the case of CoFe-N-PDC they have formed in-situ during the pyrolysis



of ZIF-8 precursor with TMs as also known from several previous investigations.^{38, 40, 52, 53, 60}

Article Online
DOI: 10.1039/D6TA01012A

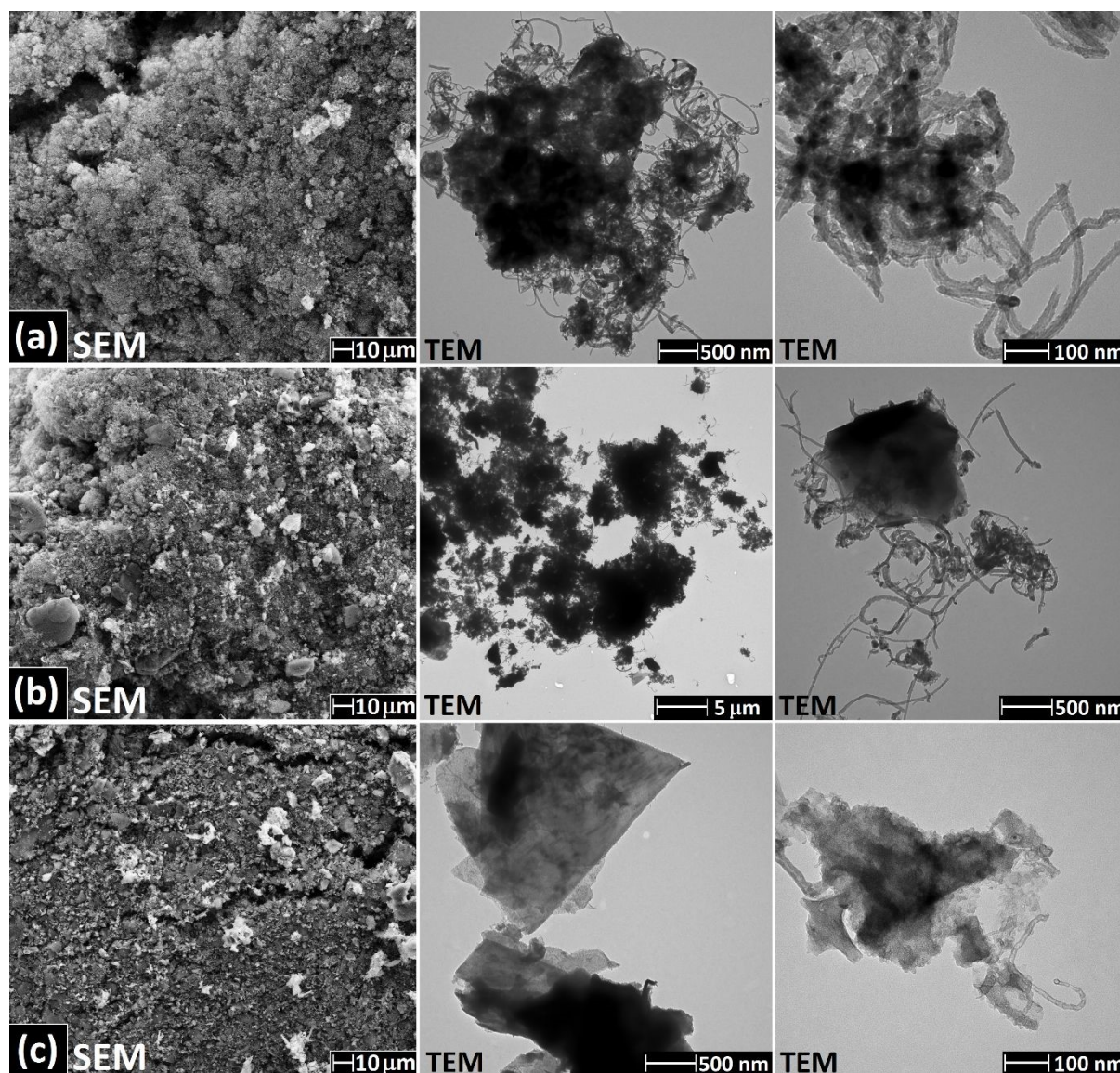


Fig. 3. SEM and TEM images of (a) CoFe-N-CNT, (b) CoFe-N-CNT/PDC, (c) CoFe-N-PDC catalysts.

The observable differences are that in the case of CoFe-N-PDC, a lower overall amount of CNTs with a smaller diameter are observed. This observation suggests that the addition of CNTs is a beneficial direction in optimising nanocarbon structures for ORR catalysts. The bulk composition of the CoFe-N-C catalysts according to the EDS studies (Table 2) showed the expected presence of N around 4 at% in all the catalysts together with 0.25-0.50 at% of total Co and Fe necessary for the $M-N_x$ formation with high ORR electrocatalytic activity.^{21, 60} The



content of Si is in accordance with the various amounts of PDC in the nanocarbon backbone while trace amounts of Zn were also observed specifically in the case when PDC is used. Since the determination of Mo content was not feasible due to the technical limitations (Au support) and the uncertainty values for TMs were considerable, then ICP-MS analyses were performed to study the TM and S content with higher precision (Table S2). The Fe, Co, Zn, and S content shows similar trends among the ICP-MS and EDS investigations, whereas the contents of Mo and S are directly dependent on the CNT amount, indicating the origin of these elements from CNTs.

Table 2 Elemental composition (at%) determined from EDS analysis for different nanocarbon backbone CoFe-N-C catalysts.

Element	CoFe-N-CNT	CoFe-N-CNT/PDC	CoFe-N-PDC
C	91.62 ± 0.68	88.32 ± 1.78	77.27 ± 1.37
N	4.63 ± 0.40	3.66 ± 0.76	4.37 ± 0.60
O	3.12 ± 0.51	5.53 ± 1.33	13.12 ± 1.08
Si	-	1.75 ± 0.51	4.98 ± 0.98
S	0.32 ± 0.07	0.24 ± 0.06	0.01 ± 0.02
Fe	0.17 ± 0.04	0.22 ± 0.11	0.15 ± 0.06
Co	0.15 ± 0.06	0.28 ± 0.22	0.10 ± 0.06
Mo	n.d.	n.d.	n.d.
Zn	-	0.01 ± 0.01	0.02 ± 0.03

To study the structure and elemental distribution in the CoFe-N-C catalysts in more detail, the HR-TEM images were collected, and the elemental mapping was performed (Figs. 4, S2-3). The HR-TEM images reveal the fine distribution of N and the presence of TM nanoparticles in the structure of all the catalysts. In more specific, the CoFe alloy nanoparticles are observed as the maps of the corresponding elements overlay and the XRD analysis revealed the reflex corresponding to the very same alloy (Fig. 2). Furthermore, the overlay of Fe and Co elemental maps could indicate the presence of Co and Fe bimetallic sites, which are highly beneficial for ORR activity.²¹ In the mapping images, the Mo nanoparticles are clearly observed in the case of CoFe-N-CNT (Fig. S2b), while their location distinctly varies from those of CoFe. This indicates that Mo is probably a residue from the commercial CNT (CP-0006-SG, IoLiTec)



fabrication procedure with relatively thick carbon coating as only the XRD reflexes for molybdenum carbide were observed (Fig. 2b). Also, the CoFe alloy nanoparticles in the catalyst materials are covered with several graphene layers (Fig. 4a), which explains their preservation after harsh acid treatment procedure in 2 M H₂SO₄ for 16h.

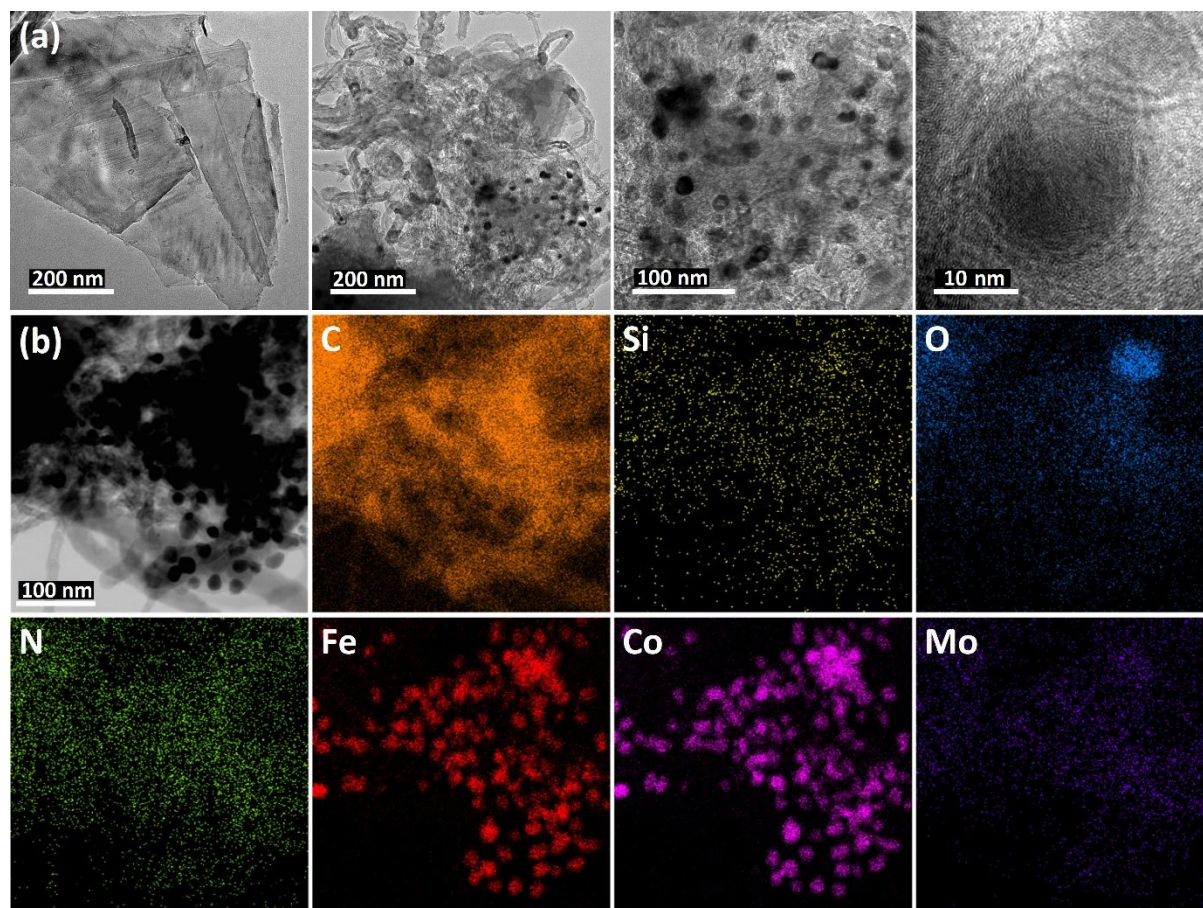


Fig. 4 Bright-field HR-TEM images for CoFe-N-CNT/PDC catalyst from (a) different magnifications and locations, (b) with TEM-EDS elemental maps.

XPS studies were performed to investigate the surface composition of the Fe-N-CNT/PDC and various CoFe-N-C catalysts (Fig. 5). From the surface of all the catalyst materials, the XP signals for Fe2p, O1s, N1s, and C1s were detected. Additionally, in the case of PDC and Co salt used in the catalyst precursor mixture, the XP signals from Si2s/2p and Co2p, respectively, were detected. No clearly distinguishable photoelectron signal for Zn over the background was detected due to the acid leaching and second pyrolysis effect known for its removal.^{38, 57, 61, 62}



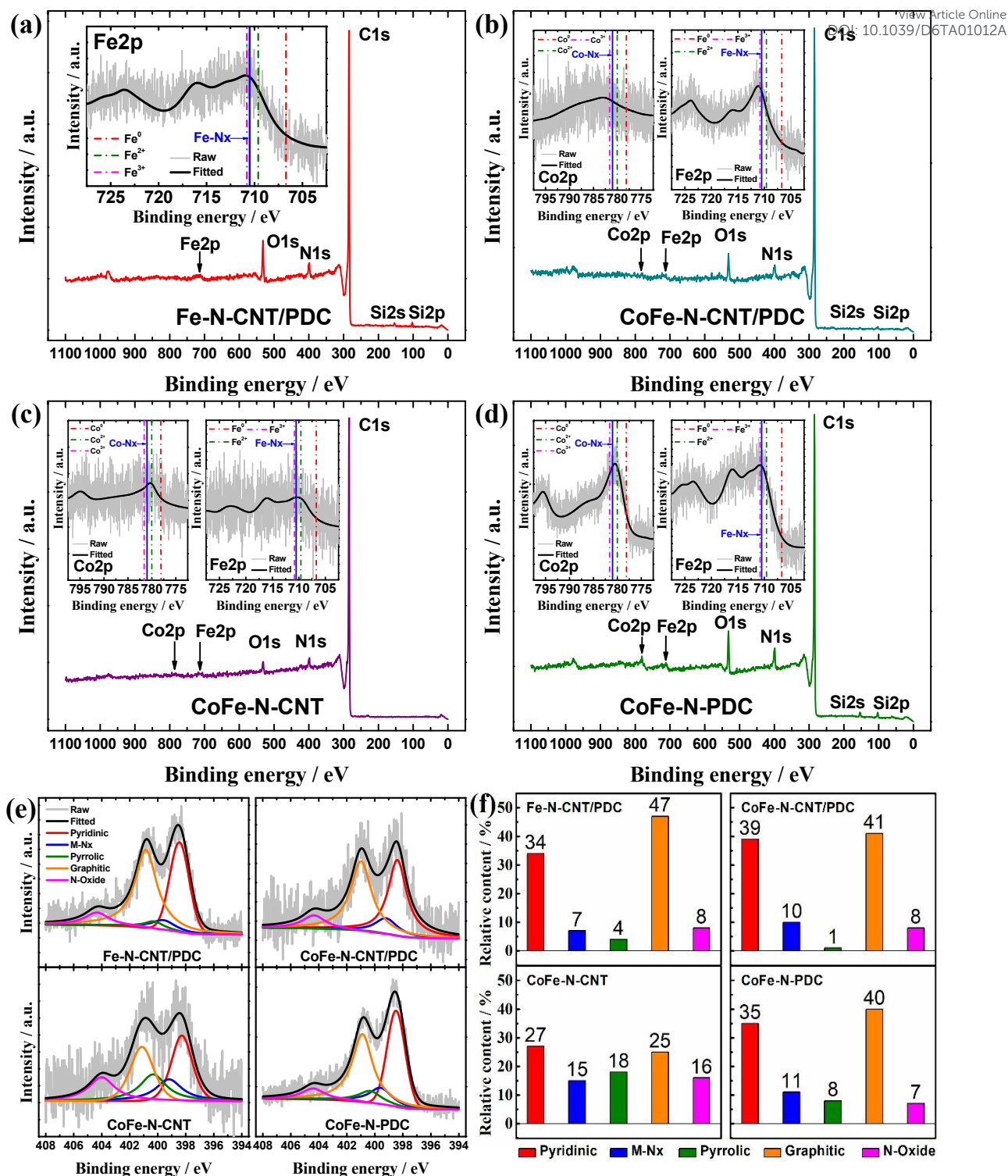


Fig. 5. (a-d) Survey XPS-spectra and high-resolution XPS-spectra of Fe2p and Co2p with indicated peak maxima of the respective oxidation states, (e, f) high-resolution XPS-spectra of N1s and relative content (rounded to an integer) of the determined nitrogen species for different M-N-C catalyst material powders.

Additionally, no distinct XPS signals for the S or Mo were detected, indicating that these elements originate from the inside of commercial CNT (Tables 2 and S2) and are not present



within the 5-10 nm depth⁶³ of the catalyst surface. The C1s XPS peak (Fig. S4) mainly corresponds to the graphitic carbon (C=C sp², ca 284.4 eV)^{64, 65} in the case of all materials, which is supported by the XRD and Raman spectroscopy results (Figs. 1a, 2 and S1) together with previous reports for various SiOC,^{42, 66} ZIF-8,^{67, 68} and CNT-based^{69, 70} catalysts prepared via pyrolysis. The highly graphitic carbon skeleton provides good electrical conductivity to the active sites for ORR.⁷¹ As expected, the amount of PDC in the nanocarbon backbone is in correlation with the higher amount of C-O (ca 286.2 eV) and C=O (ca 287.3 eV) bonds in the C1s spectrum originating from the SiOC structure in the case of CoFe-N-C catalysts (Fig. S4). The deconvolution of N1s spectra to 5 different N species can provide important information about the presence of the active sites for ORR in the catalysts (Figs. 5e-f).^{38, 72} As a common observation among all materials, the highest relative content is observed for pyridinic-N (27-39%, ca 398.3 eV) and graphitic-N (25-47%, ca 401.0 eV). Those two N species are considered the most important for providing high activity towards ORR, as the pyridinic-N with a lone pair of electrons can favour the adsorption of O₂ or OOH, and graphitic-N enhances the electronic conductivity.^{68, 73, 74} Furthermore, the pyrrolic-N (ca 400.3 eV) and especially M-N_x (ca 399.2 eV)^{29, 32, 75, 76} species are also of utmost importance, as due to their close binding energy peak values and peak overlapping, they are very difficult to be clearly distinguished from each other. For example, in the investigation of dual TM catalyst FeCu-N-C by Hao et al.,⁷⁷ the admirable ORR activity and stability were mainly attributed to the pyrrolic-N-type of Fe-N₄ sites. To further evaluate the presence of M-N_x sites in the (Co)Fe-N-C materials prepared herein, the high-resolution XP spectra in Fe2p and Co2p region were recorded and studied (Figs. 5a-d, S5). Due to the modest Fe/Co bulk content (Table 2) and acid leaching procedure, the weak XP signals of these TMs are collected from the catalyst surface with a low signal-to-noise ratio (SNR). Therefore, determining the surface metal content (at%) is not adequate due to the SNR's influence on the deconvolution procedure (Fig. S5).^{78, 79} In this



situation, it is feasible to determine the locations of the maxima for the Fe and Co XP peaks with different oxidation states, which have been cross-checked with literature sources (Figs. 5a-d).^{38, 48} It can be concluded that the Fe and Co atoms on the material surface are rather in oxidation states (+II/+III) and not metallic (0). This is supported using a strong acid treatment, which can oxidise any 0-valent TM and wash the TM species away from the surface and outside of the graphitic layer-protected TM nanoparticles (Figs. 4, S2-3).⁸⁰ The M-N_x species are known to be resistant to acid leaching⁸¹ and the XP peak maxima in Fe2p and Co2p spectra are recorded herein close to the previously reported values for Fe-N_x (ca 710.5 eV) and Co-N_x (ca 781.0 eV).^{57, 82, 83} Among the oxidation states of +II and +III, the bivalent (+II) is reported to provide the active TM site for ORR in the M-N_x.^{32, 84} However, it should also be pointed out that the very close values and overlapping of the peaks +II/-N_x/+III create a somewhat similar situation in their specific distinction as the difficulty of peak separation observed in N1s spectra for pyridinic-N/M-N_x/pyrrolic-N (Fig. 5e). Still based on the XPS data collected herein, it would be safe to assume the verified existence of M-N_x, especially if the harsh acid treatment procedure within the fabrication process of the catalysts is considered (Section 2.1). In addition to individual Fe-N_x and Co-N_x sites, some of the M-N_x could be in the Co-Fe dual-atom configuration, which would be highly desirable for high ORR electrocatalytic activity.^{26, 30} Unfortunately, the XPS cannot unambiguously distinguish between single-atom and dual-atom M-N_x sites.

3.2. Half-cell oxygen reduction studies using RRDE and HT-GDE methods

The activity towards ORR of the prepared M-N-C catalysts was first evaluated using RRDE in 0.5 M H₃PO₄ environment as known to be suitable for non-PGM cathode materials with HT-PEMFC target application.^{78, 85} According to one of the main aims of this investigation, the different nanocarbon backbone CoFe-N-C catalysts were firstly compared (Figs. 6a and b,



Table 3). The half-wave potential ($E_{1/2}$) and current density at 0 V ($j@0V$) values of CoFe-N-PDC are very similar to those of CoFe-N-SiOCa (0.4 mg cm⁻²) from our previous investigation,³⁸ where Co and Fe salts were incorporated into the initial PDC precursor composition and not later during the ultrasonic mixing with ZIF-8. The addition of CNT into the backbone leads to different effects. Firstly, the $j@0V$ value increases with a higher proportion of CNTs, which is a beneficial observation for enhanced ORR activity. Simultaneously, a lower $E_{1/2}$ is observed, accompanied by a higher H₂O₂ yield between 0.3 and 0.8 V, which can be considered a negative effect on the ORR performance. For comparison, the Co-free derivative of CoFe-N-CNT/PDC was prepared to investigate the influence of Co inclusion (Fe-N-CNT/PDC). In 0.5 M H₃PO₄ solution at RT, there is no benefit of Co inclusion into the M-N-C composition for the ORR performance. This is an expected result as in these conditions Co-N_x sites are known to catalyse ORR via 2e⁻ pathway, while Fe-N_x catalyse the 4e⁻ route.^{31, 82} The mass activity value at 0.8 V (MA@0.80V) of 1.6 A g⁻¹ for Fe-N-CNT/PDC is in a similar range as the values reported for HNO₃-treated and carbon aerogel-based Fe-N-C in a parallel investigation by Zierdt et al.⁷⁸ Additionally, as the binary TM combination of Mn/Fe was found to be beneficial for obtaining low H₂O₂ yield in our previous study of PDC/ZIF-8 catalysts, then the Mn-containing derivatives of CoFe-N-CNT/PDC and Fe-N-CNT/PDC were also prepared and investigated using the RRDE technique (Figs. S6a and b, Table 3). The inclusion of Mn decreased the H₂O₂ yield as expected, while having no noticeable effect on the $E_{1/2}$ and $j@0V$ values, and finally decreasing the MA@0.80V value compared to the Fe-N-CNT/PDC. In the RRDE conditions, the commercial Fe-N-C (PMF-011904, Pajarito Powder, LLC) outperformed all the M-N-C catalysts prepared herein, which is similar to our previous investigation of binary TM combination ZIF-8/PDC catalysts.³⁸ As a main reason, the higher ORR performance of Fe-N-C can be explained by the considerably higher SSA as determined in a latter study ($S_{BET} = 597.7 \text{ m}^2 \text{ g}^{-1}$).³⁸ Compared to the alternative bimetal M-N-

View Article Online
DOI: 10.1039/D6TA01012A



C investigated using RRDE in 0.5 M H₃PO₄ for HT-PEMFC target application, the recent ZIF-8 derived Fe–Sn–N–C (1:0.3) exhibiting the remarkable MA@0.80V of 19.3 A g⁻¹ should be outlined from a recent investigation by Buschermöhle et al.⁴⁸

As the long-term stability of the M-N-C is one of the most important issues in HT-PEMFC conditions, the accelerated durability test (ADT) protocol of 24 hours in 0.5 M H₃PO₄ from our previous study³⁸ was implemented (Fig. S7). The smallest decline in $E_{1/2}$ value after 10 000 CV cycles was observed for the CNT-free CoFe-N-PDC catalyst ($\Delta E_{1/2} = 21$ mV), which is in good accordance with the older investigation (CoFe-N-SiOCa)³⁸ and refers to the PDC nanocarbon backbone's good durability. In the case of CNT/PDC-based materials, the higher $\Delta E_{1/2}$ of 54 is observed in the case of Fe-N-CNT/PDC compared to the $\Delta E_{1/2}$ of 48 for CoFe-N-CNT/PDC. This could indicate the scavenging of ROS due to the inclusion of Co-N_x or Fe/Co-N_x sites compared to the only Fe-containing M-N-C.^{23, 25} For the catalyst-coated RRDE disc areas, the SEM measurements and EDX analysis can also be performed before and after implementing the ADT (Fig. S8 and Table S3). SEM images show no visible differences before and after stability testing, whereas EDX analysis reveals some differences. For both studied CoFe-N-C samples, a similar decrease in the Fe and Co content is observed, most likely due to demetallation of M-N_x sites during the ADT. At the same time, the amount of Mo does not decrease, confirming that Mo is not at the center of the M-N_x sites on the catalyst surface, but is rather hidden inside the nanotubes and therefore inactive for the surface reactions. The new component F, which was not observed during the original physical characterisation of the M-N-C in Section 3.1, originates from the Nafion[®] binder.

Furthermore, the CV responses of the prepared M-N-C catalysts were recorded using a potential scan rate of 50 mV s⁻¹ in Ar- and O₂-saturated 0.5 M H₃PO₄ (Fig. S9). The determined ORR peak potentials (E_p) follow the same general trend as observed for the $E_{1/2}$ values for the RRDE measurements (Table 3). However, the highest E_p value of 0.69 V of CoFe-N-PDC



outperforms the $E_p = 0.65$ V determined in the previous investigation for both, CoFe-N-SiOCa and commercial Fe-N-C,³⁸ indicating that CoFe-N-PDC is a superior ORR electrocatalyst in these specific conditions of CV measurements. This is very likely an overevaluation as RRDE results are more reliable due to the benefits of hydrodynamic conditions, iR-drop correction, and the removal of the background current.

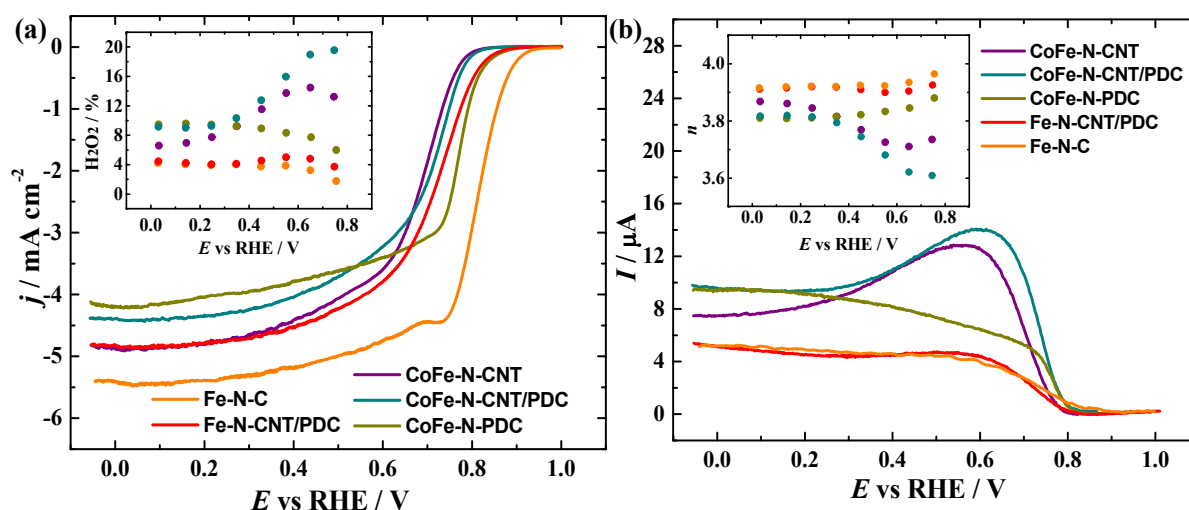


Fig. 6. Polarisation curves recorded with RRDE method for (a) oxygen reduction at disc, (b) H_2O_2 oxidation at ring on different M-N-C coated GC-disc with Pt-ring electrode in O_2 -saturated 0.5 M H_3PO_4 at 1600 rpm and 10 mV s^{-1} . The insets show (a) peroxide yield (%) and (b) electron transfer number (n) as a function of potential.

Table 3. Oxygen reduction half-wave potential ($E_{1/2}$), current density at 0 V ($j@0\text{V}$), mass activity values at 0.8 V ($\text{MA}@0.80\text{V}$), average electron transfer number (n), average peroxide yield (H_2O_2) obtained from RRDE voltammetry disc and ring curves at 1600 rpm in O_2 -saturated 0.5 M H_3PO_4 . All the values have been obtained from the iR-drop corrected I - E curves recorded with the M-N-C loading of 0.4 mg cm^{-2} shown in Figs. 6 and S6.

Catalyst	$E_{1/2}$ (V vs RHE)	$j@0\text{V}$ (mA cm^{-2})	$\text{MA}@0.80\text{V}$ (A g^{-1})	n	H_2O_2 (%)
CoFe-N-PDC	0.76	-4.2	2.4	3.8	8.6
CoFe-N-CNT/PDC	0.70	-4.4	0.4	3.7	13.1
CoFe-N-CNT	0.68	-4.9	0.2	3.8	10.4
Fe-N-CNT/PDC	0.71	-4.8	1.6	3.9	4.4
MnFe-N-CNT/PDC	0.70	-4.7	1.1	3.9	4.1
CoMnFe-N-CNT/PDC	0.71	-4.4	0.7	3.8	8.2
Fe-N-C	0.80	-5.4	16.0	3.9	3.6



From the HT-PEMFC target application point of view, the ORR investigations in HT-GDE are considerably closer to the real device conditions compared to the RRDE conditions at RT. Therefore, all the M-N-C prepared in this work and Fe-N-C for comparison were further evaluated in the HT-GDE setup as ORR catalysts (Figs. 7 and S10, Table 4). Firstly, the HT-GDE setup modifications implemented in the present investigation were evaluated using the commercial Fe-N-C catalyst. In a previous study using a Cu current collector (CC) and a catalyst loading (CL) of 3.0 mg cm^{-2} , the open-circuit potential (OCP) and potential value at 187 mA cm^{-2} (E_{187}) were recorded as 865 ± 24 and 421 ± 27 mV, respectively.³⁸ Herein, considerably higher activity towards the ORR was observed for Fe-N-C with an OCP = 905 ± 5 and $E_{187} = 510 \pm 52$ mV, which can be attributed to the use of stainless steel CC and CL of 4.2 mg cm^{-2} (Section S3). In addition to the influence of higher CL, it is likely that Cu ions from CC can poison the PA-PBI membrane as supported by corresponding information published for Nafion™ membranes in LT-PEMFC application.⁸⁶ According to the already discussed RRDE results, there was no observable difference in the ORR activity of the final catalysts if the Co and Fe salts are incorporated into the initial PDC precursor (CoFe-N-SiOCa)³⁸ or later during the ultrasonic mixing step (CoFe-N-PDC, this work). In the case of the HT-GDE setup, the situation is different as CoFe-N-SiOCa tested with Cu CC and lower CL showed $E_{187} = 360 \pm 27$ mV,³⁸ while only $E_{187} = 306 \pm 30$ was recorded for CoFe-N-PDC herein. This considerable difference in the ORR performance between RRDE and HT-GDE for otherwise identical catalysts may result from the large difference in temperature and electrolyte acid concentration, showing the superiority of HT-GDE testing if HT-PEMFC is the target application. The inclusion of CNT into the CoFe-N-C catalyst composition causes an increase in the ORR activity, which is so significant that CoFe-N-CNT/PDC outperforms Fe-N-C at potential values less than ca 0.3 V. If the nanocarbon backbone consists only of CNT without any PDC, then the ORR performance decreases in the potential range relevant for real-life fuel

New Article Online
DOI: 10.1039/D6TA01012A



cell applications (higher than ca 0.5 V, Figs. 7b-c).² The collected HT-GDE data indicate that the CNT/PDC composite could be a more suitable backbone for HT-PEMFC cathode M-N-C material development than PDC or CNT alone. To assess the benefit of Co in CoFe-N-CNT/PDC composition, the HT-GDE curve of Fe-N-CNT/PDC can be studied. The commercial Fe-N-C outperforms the Fe-N-CNT/PDC throughout the ORR polarisation curve, while the superiority of Fe-N-CNT/PDC over CoFe-N-CNT/PDC is observed in the low polarisation current region between 0 and -50 mA cm⁻² (Figs. 7b-c). The latter is in accordance with the RRDE results as this method operates in similar low *j* conditions if a 10× difference in CL value is considered (Fig. 6). Furthermore, in the case of Mn-containing catalysts, the RRDE and HT-GDE results follow the very same trend with Fe-N-CNT/PDC supremacy (Fig. S10, Table 4). At higher polarisation current region, the superiority of CoFe-N-CNT(/PDC) over other M-N-C is clearly observed in the case of calculated power density curves (Fig. 7d). The maximum power density (P_{\max}) of Fe-N-C is obtained at ca 153 mW cm⁻², which is in good accordance with the previous HT-GDE investigations with ultrasonic spray-coated Fe-N-C catalyst exhibiting 142 mW cm⁻².⁸⁷ In the case of CoFe-N-CNT(/PDC), the P_{\max} of ca 188 mW cm⁻² is obtained (Table 4), which indicates that these catalysts are the most suitable for the application at the HT-PEMFC cathode in this work.

View Article Online
DOI: 10.1039/D6TA01012A



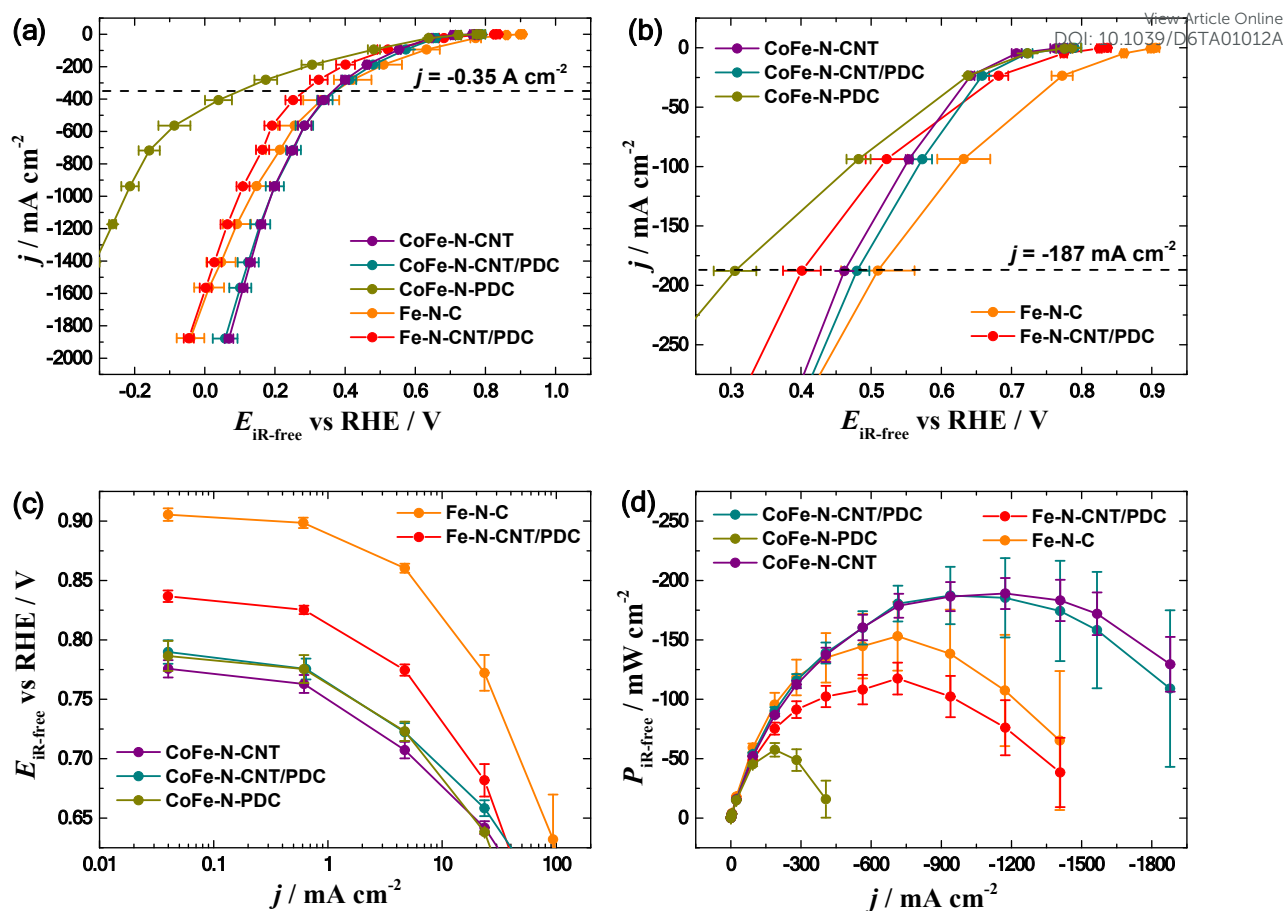


Fig. 7. (a, b) HT-GDE half-cell polarisation curves of M-N-C coated (4.2 mg cm^{-2}) GDEs for ORR measured using the O_2 flow rate 0.15 L min^{-1} , 160°C , conc. H_3PO_4 , PA-PBI membrane. (c) Semi-logarithmic plots of the polarisation curves and (d) calculated power density curves.

The trend of ORR activity is similar among CoFe-N-CNT(PDC) and Fe-N-C catalysts between RRDE (Fig. 6a) and HT-GDE setup within a polarisation current density range from 0 to -0.35 A cm^{-2} (Fig. 7a). Between -0.35 and 1.9 A cm^{-2} , the superior ORR performance of CoFe-N-CNT(PDC) over Fe-N-C could be due to the change in deactivation mechanisms of M-N-C cathodes during PEMFC operation at HT influencing the M-N-C stability compared to the RRDE experiments at RT according to the investigation by Bae et al.⁸⁸ Also, the synergistic effect between Fe-N_x and Co-N_x or Fe/Co-N_x could be amplified due to the HT conditions improving the activity towards the ORR. The CVs recorded before and after the measurements for HT-GDE half-cell polarisation curves are shown in Fig. S11 for Fe-N-C and CoFe-N-



CNT/PDC. In this work, the CVs recorded before and after are considerably more similar indicating that the GDE system is less influenced by the tests compared to the previous investigation.³⁸ This difference could be favoured by the higher CL and stainless steel CC used in the present study. The lower capacitive current under the CV of CoFe-N-CNT/PDC compared to that of Fe-N-C is consistent with the higher SSA of the latter catalyst.

Table 4. HT-GDE half-cell testing results, open circuit potential (OCP), potential value at 187 mA cm⁻² (E_{187}), maximum power density (P_{\max}) normalised to the surface area and M-N-C weight using the M-N-C loading (4.2 mg cm⁻²) for ORR derived from the HT-GDE polarisation curves with different M-N-C shown in Figs. 7 and S10.

Catalyst	OCP (mV vs RHE)	E_{187} (mV vs RHE)	P_{\max} (mW cm ⁻²)	P_{\max} (W g _{Catalyst} ⁻¹)
Fe-N-C	905 ± 5	510 ± 52	153 ± 29	36 ± 7
Fe-N-CNT/PDC	837 ± 5	401 ± 27	117 ± 13	28 ± 3
MnFe-N-CNT/PDC	813 ± 2	337 ± 27	77 ± 14	18 ± 3
CoMnFe-N-CNT/PDC	808 ± 1	404 ± 17	112 ± 10	27 ± 2
CoFe-N-CNT/PDC	790 ± 10	480 ± 18	187 ± 24	45 ± 6
CoFe-N-CNT	776 ± 7	462 ± 7	189 ± 13	45 ± 3
CoFe-N-PDC	786 ± 13	306 ± 30	57 ± 6	14 ± 1

One of the major issues for M-N-C catalysts in HT-PEMFC is the stability due to the harsh conditions, and the ADT protocol used for 0.5 M H₃PO₄ solution, including RRDE and 10 000 CV experiments (Fig. S7), could underestimate the M-N-C stability due to the lower temperature and lower acid concentration.^{13, 23, 43} Therefore, the stability testing procedure in HT-GDE setup was implemented for the very first time using chronopotentiometry with a constant current value of 0.1 A cm⁻² from earlier Fe-N-C stability investigation at the HT-PEMFC cathode.²³ The testing was carried out over 3 hours with EIS measurement after every 20 minutes to include the iR -drop correction data throughout the measurement (Fig. 8). As expected, the obtained results indicate the observable decline in the ORR performance of M-N-C, similar to the case of the ADT protocol used in 0.5 M H₃PO₄. The Fe-N-C exhibited the highest ORR voltage loss of 80 mV over the experiment, while still being the most active catalyst after the testing, final $E_{iR-free} = 0.51$ V. All other M-N-C materials exhibited a voltage



loss between 30–60 mV, with the highest final $E_{iR\text{-free}}$ of 0.48 and 0.46 V for CoFe-N-CNT/PDC and CoFe-N-CNT, respectively. On the other hand, when both CNT-containing CoFe-N-C showed similar voltage loss of ca 60 mV, then the CoFe-N-PDC showed only 36 mV (Fig. 8b). This situation is similar to the lowest $\Delta E_{1/2}$ value observed for CoFe-N-PDC after ADT in 0.5 M H_3PO_4 solution among different CoFe-N-C (Fig. S7). In conclusion, the superior durability of PDC over CNT in the M-N-C backbone was verified under both durability testing conditions, using the RRDE technique at RT (24 h) and the HT-GDE half-cell at 160 °C (3 h). The considerably higher voltage loss of Fe-N-CNT/PDC (60 mV) compared to the lowest registered voltage loss for CoMnFe-N-CNT/PDC (30 mV) in Fig. 8a, can indicate that Co-N_x and Mn-N_x could help to prevent the formation or scavenge ROS from Fe-N_x sites in HT conditions, but proving this would require further experimental verification. The short 3-hour period for the stability test is due to the HT-GDE setup's operating limitations, while it still describes the most rapid ORR activity loss region of M-N-C according to published HT-PEMFC results.^{23, 88}

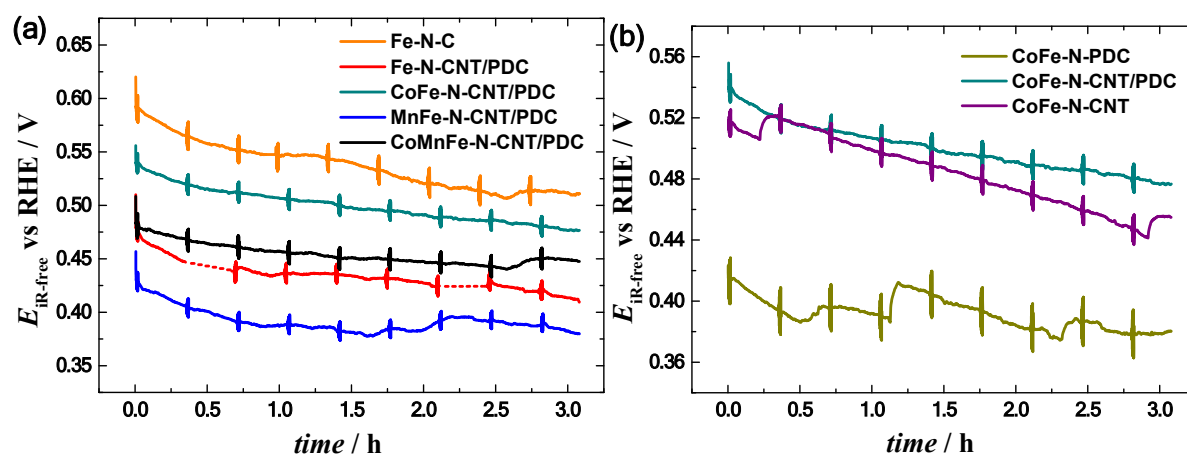


Fig. 8. Chronopotentiometry measurements at 0.1 A cm⁻² using HT-GDE half-cell setup with M-N-C coated (4.2 mg cm⁻²) GDEs for ORR measured using the O₂ flow rate 0.15 L min⁻¹, 160 °C, conc. H₃PO₄, PA-PBI membrane. EIS measurements were performed after every 20 minutes.

If the CVs recorded before and after the 3-hour test are compared, the appearance of redox peaks at ca 0.25 and 0.5 V is observed in the case of multiple metal co-doped M-N-C compared



to the Fe-N-C and Fe-N-CNT/PDC (Figs. S12 and S13). Both responses could correspond to the electrochemical transitions in TM (alloy) nanoparticles (e.g. Fe²⁺/Fe³⁺), which were observed during the HR-TEM experiments (Figs. 4, S2-3).^{78, 89, 90} Whereas, the redox response at 0.5 V can also include the hydroquinone/quinone (HQ/Q) species introduced due to the carbon corrosion.^{23, 29, 87} The 3-hour operating data show that CoFe-N-CNT(/PDC) and Fe-N-C could be the most promising for the HT-PEMFC cathode among the M-N-C catalysts studied herein.

3.3. HT-PEMFC testing

Single-cell tests were conducted with the three pre-selected (Section 3.2) cathode catalysts (CoFe-N-CNT(/PDC), Fe-N-C), PA-PBI membrane, and commercial Pt/C anode. In this work, the M-N-C catalysts were drop-cast onto the cathode GDL resulting in a CL of 3.5 mg cm⁻². The data obtained for HT-PEMFC tests are shown in Fig. 9 and Table 5. Firstly, the results for commercial Fe-N-C ($P_{100} = 62 \text{ mW cm}^{-2}$, $P_{\text{max}} = 134 \text{ mW cm}^{-2}$) are in accordance with the previous data (CL = 3.1-3.5 mg cm⁻², $P_{100} = 53\text{-}56 \text{ mW cm}^{-2}$, $P_{\text{max}} = 140\text{-}155 \text{ mW cm}^{-2}$) reported for ultrasonically coated and doctor-bladed Fe-N-C cathodes investigated in HT-PEMFC in an earlier investigation.⁹⁰ Both CoFe-N-C catalysts exhibit lower HT-PEMFC current density than Fe-N-C, especially at 0.65-0.7 V and up near the activation polarisation region, which voltages are important for LDV and HDV applications point of view.² This observation is in accordance with the HT-GDE results, where Fe-N-C outperformed CoFe-N-C in the low polarisation current density range (-0.35 to 0 A cm⁻², Fig. 7). The observed difference in the higher polarisation current density region, where compared to HT-GDE tests, Fe-N-C is still more active than both CoFe-N-C, could be due to the different acid wetting conditions of the PA-PBI membrane in these devices and a 20% higher amount of catalyst at the HT-GDE cathode.



The overall superior HT-PEMFC performance of Fe-N-C over CoFe-N-CNT(/PDC) can be first attributed to its higher OCV value, likely due to the higher intrinsic activity and better accessibility of the Fe-N_x sites in Fe-N-C. Secondly, the lowest ohmic resistance for Fe-N-C (Fig. 9c) indicates a better electrical conductivity and/or more successful integration with the PA-PBI membrane in the case of Fe-N-C. Thirdly, similarly to the HT-GDE tests (Figs. S11-S13), the highest surface area under the CV curve (Fig. 9d) is also observed in the case of Fe-N-C, which is supported by the considerably higher S_{BET} value ($597.7 \text{ m}^2 \text{ g}^{-1}$)³⁸ compared to CoFe-N-CNT(/PDC) (Table 1). Also, the lower area under the CV curve for CoFe-N-CNT(/PDC) could indicate a lower acid coverage, leading to fewer accessible active sites than in Fe-N-C. Between CoFe-N-C catalysts, the CoFe-N-CNT shows superior performance at j values more than 100 mA cm^{-2} , and the CoFe-N-CNT/PDC between $j = 0$ and ca 25 mA cm^{-2} . The latter region of low j is more important from a practical application point of view as this region corresponds to 0.6-0.8 V.²

View Article Online
DOI: 10.1039/D6TA01012A



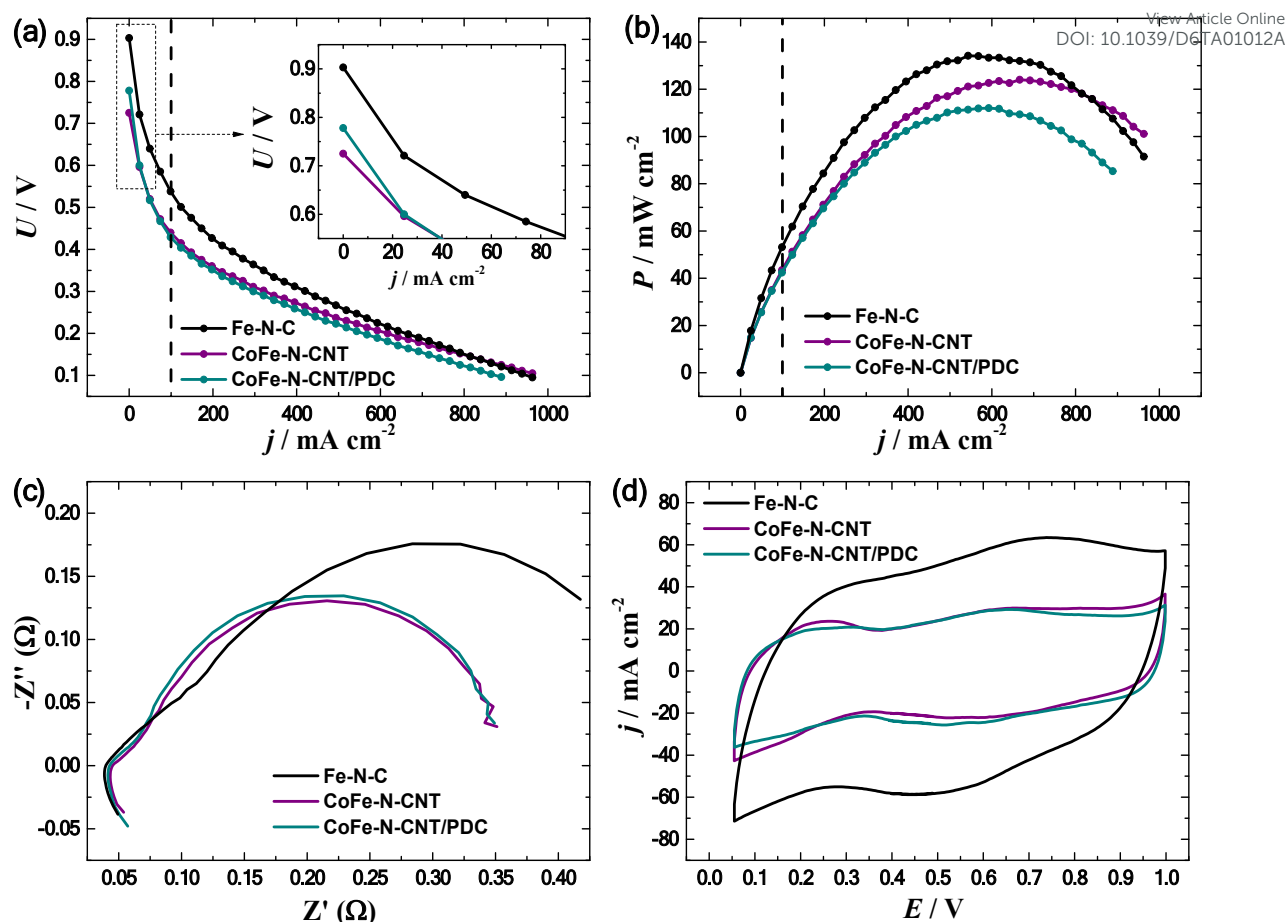


Fig. 9. HT-PEMFC measurements with M-N-C cathode catalysts (3.5 mg cm^{-2}), (a) galvanostatic polarisation curves and (b) calculated power density curves recorded under H_2/O_2 (1.5/9.5) at 160°C , (c) Nyquist plots from EIS at 0.1 A cm^{-2} recorded with dry H_2/O_2 (1.5/9.5), (d) CVs recorded under H_2/N_2 flow rate of 0.1 L min^{-1} and scan rate of 100 mV s^{-1} .

There is no prior knowledge of any CoFe-N-C application at the HT-PEMFC cathode besides our own previous work, where CoFe-N-SiOCa with only a PDC-based backbone³⁸ showed inferior performance compared to both CoFe-N-CNT(PDC) tested herein (Table 5). The incorporation of Co into the M-N-C catalyst composition for HT-PEMFC is strongly supported by a study by Eren et al.,⁷⁰ where the Co-N/MWCNT cathode fed with dry air showed a remarkable P_{100} of 52 mW cm^{-2} . Among bimetallic M-N-C catalysts, the state-of-the-art at 160°C operation is currently the FeCu(4:1) catalyst by Cheng et al.,⁹¹ reported with the P_{100} and P_{max} of 68 and 250 mW cm^{-2} , respectively, in the HT-PEMFC conditions with an improved SiO_2 -doped PA/PBI composite membrane. Nevertheless, the novel CoFe-N-CNT/PDC



catalyst prepared herein for the HT-PEMFC cathode outperforms several previously developed bimetallic M-N-C catalysts (Table 5).

Table 5. HT-PEMFC testing results with various M-N-C cathodes performed in this investigation and from the previous literature reports, open-circuit voltage (OCV), power density at 100 mA cm⁻² (P_{100}), maximum power density (P_{max}), and cell temperature (T). All results are reported for PA-PBI membrane and Pt/C anode catalyst-based MEAs operated with dry O₂/H₂ gases.

Cathode catalyst	OCV (V)	M-N-C loading (mg cm ⁻²)	P_{100} (mW cm ⁻²)	P_{max} (mW cm ⁻²)	T (°C)	Reference
Fe-N-C	0.90	3.5	62	134	160	This work
CoFe-N-CNT/PDC	0.78	3.5	42	112	160	This work
CoFe-N-CNT	0.73	3.5	43	124	160	This work
CoFe-N-SiOCa	0.77	3.0	34	50	160	38
Co-N/MWCNT	0.96 ^b	3.0	52 ^{a,b}	66 ^b	160	70
Fe-Sn-N-C	0.86	3.1	35	53	160	48
Fe-N-ox-BP	0.82	3.1	39	67	160	23
FeCu(4:1)	-	4.0	68 ^a	250	160	91
FeCu(4:1)	0.88	4.0	75 ^a	302	230	91

^aValues determined from the figures provided in the paper.

^bExperiment performed with dry air fed to the cathode instead of O₂ gas.

4. Conclusions

In the present investigation, a double TM and N-functionalised M-N-C catalyst with an optimised nanocarbon backbone was developed for the HT-PEMFC cathode. The preliminary testing of different M-N-C materials towards the ORR activity was performed comparably using RRDE technique at RT and HT-GDE half-cell at 160 °C. The RRDE tests in 0.5 M H₃PO₄ solution showed the superiority of PDC as a single backbone component catalyst (CoFe-N-PDC) according to the $E_{1/2}$ value of 0.76 V vs RHE and MA@0.80V of 2.4 A g⁻¹. In the HT-GDE conditions, the CoFe-N-CNT/PDC and CoFe-N-CNT showed remarkable ORR activity by outperforming even the commercial Fe-N-C in the $j = -0.35$ to -1.9 A cm⁻² range. The P_{max} values around 188 mW cm⁻² were obtained with both CoFe-N-CNT(/PDC) catalysts compared to the Fe-N-C (153 mW cm⁻²) in HT-GDE conditions. The 3-hour durability test at constant



current of 100 mA cm^{-2} in HT-GDE showed an ORR voltage loss of 80 mV for Fe-N-C, while the corresponding value for CoFe-N-CNT/PDC and CoFe-N-CNT was ca 60 mV. The superior durability of PDC as the M-N-C backbone component was observed in two different types of durability testing conditions, using the RRDE technique with 10 000 CV cycles (CoFe-N-PDC, $\Delta E_{1/2} = 21 \text{ mV}$) and the HT-GDE half-cell 3-hour test at 100 mA cm^{-2} (CoFe-N-PDC, voltage loss = 36 mV). One of the reasons for the decrease in ORR activity of CoFe-N-C catalysts was found as demetallation of M-N_x sites, which was confirmed by EDX analysis before and after the ADT in RRDE conditions. On the other hand, HT-GDE tests indicated that the inclusion of Co and Mn into the M-N-C catalyst could help to scavenge or reduce the ROS production at Fe-N_x sites. During application at the HT-PEMFC cathode, the overall superiority of Fe-N-C was witnessed ($P_{\text{max}} = 134 \text{ mW cm}^{-2}$), while the corresponding values for CoFe-N-C reached 83-93% of the Fe-N-C. In the voltage range relevant to LDV and HDV applications, the CoFe-N-CNT/PDC outperformed the CoFe-N-CNT. The high activity towards the ORR of the prepared catalysts was mainly attributed to the presence of Fe-, Co-, N-based active sites (e.g. Co-N_x, Fe-N_x, pyridinic-N, graphitic-N) detected in the nanocarbon matrix and TM (alloy) NPs by XPS and TEM techniques. The inclusion of CNT together with PDC into the nanocarbon backbone of the M-N-C increased the SSA, enabling the fabrication of an optimal CoFe-N-CNT/PDC catalyst for the HT-PEMFC application.

Conflicts of interest

There are no conflicts to declare.

Acknowledgements

This study was financially supported by the Estonian Research Council grant (PUTJD1170). M. M. acknowledges DLR and the German Academic Exchange Service



(DAAD) for the funding via DLR-DAAD Research Fellowship No. 521. The XPS instrument is funded by German Research Foundation (DFG) through grant INST 184/144-1 FUGG. The authors acknowledge the Electron and Light Microscopy Service Unit of the School of Mathematics and Science of the Carl von Ossietzky University for the use of the imaging facilities. The authors acknowledge the opportunity to conduct Raman measurements at the University of Oldenburg in the working group of Christian Schneider, with assistance from Nico Ruskaup. This research was also supported by the Estonian Ministry of Education and Research (TK210, Centre of Excellence in Sustainable Green Hydrogen and Energy Technologies). We would like to thank the following experts at the University of Tartu, Jaan Aruväli for conducting the XRD analyses, Marian Külaviir and Dr. Peeter Paaver for performing the ICP-MS analyses, Dr. Vambola Kisand and Markus Otsus for performing SEM-EDX measurements.

References

1. E. Eikeng, A. Makhsoos and B. Pollet, *Int. J. Hydrog. Energy*, 2024, 71, 433-464.
2. G. Yang, C. Lee, X. Qiao, S. Babu, U. Martinez and J. Spendelow, *Electrochem. Energy Rev.*, 2024, 7, 9.
3. S. Kazula, S. de Graaf and L. Enghardt, *J. Glob. Power Propuls. Soc.*, 2023, 7, 43-57.
4. D. Gopalasingam, B. Rakhshani and C. Rodriguez, *Hydrogen*, 2025, 6, 92.
5. F. Franke, A. Link and S. Kazula, *CEAS Aeronaut. J.*, 2025, DOI: 10.1007/s13272-13025-00908-13270.
6. A. Zucconi, J. Hack, R. Stocker, T. A. M. Suter, A. J. E. Rettie and D. J. L. Brett, *J. Mater. Chem. A*, 2024, 12, 8014-8064.
7. A. Belmesov, L. Shmygleva, A. Baranov and A. Levchenko, *Russ. Chem. Rev.*, 2024, 93, RCR5121.
8. W. Li, X. Luo, Y. Zhou, J. Shen, Y. Chen, Y. Liu and J. Qiao, *Process Saf. Environ. Protect.*, 2025, 199, 113837.
9. F. Kourougianni, A. Arsalis, A. Olympios, G. Yiasoumas, C. Konstantinou, P. Papanastasiou and G. Georghiou, *Renew. Energy*, 2024, 231, 120911.
10. Z. Xia, X. Zhang, X. Xu, J. Huang, C. Zhuang, J. Wang, S. Yu, S. Wang and G. Sun, *Appl. Catal. B-Environ. Energy*, 2025, 371, 125282.
11. S. Choi, I. Jang and S. Lee, *Crystals*, 2025, 15, 129.
12. L. Gong, L. Tao, L. Wang, X. Fu and S. Wang, *Chin. J. Catal.*, 2025, 68, 155-176.
13. N. Narayanan, B. Ravichandran, I. Emayavaramban, H. Liu and H. Su, *Catalysts*, 2025, 15, 775.
14. J. M. Linge, X. Lyu, H. Yu, H. Meyer III, M. Lehmann, T. Saito, D. Cullen and A. Serov, *Johns. Matthey Technol. Rev.*, 2025, 70, e70302.
15. J. Wang, B. Liu, X. Wang, S. Lu, Y. Xiang and J. Zhang, *J. Power Sources*, 2025, 645, 237178.



16. J. Müller-Hülstede, L. Uhlig, H. Schmies, D. Schonvogel, Q. Meyer, Y. Nie, C. Zhao, J. Vidakovic and P. Wagner, *ChemSusChem*, 2023, 16, e202202046. View Article Online
DOI: 10.1039/D3TA01012A
17. I. Sebbani, M. Ettouhami and M. Boulakhbar, *Clean. Energy Syst.*, 2025, 10, 100168.
18. N. Seselj, S. M. Alfaro, E. Bompolaki, L. N. Cleemann, T. Torres and K. Azizi, *Adv. Mater.*, 2023, 35, 2302207.
19. Q. Meyer, C. J. Yang, Y. Cheng and C. Zhao, *Electrochem. Energy Rev.*, 2023, 6, 16.
20. C. Yue, W. Zheng, Q. Wang, Z. Wang, B. Li, C. Zhang and P. Ming, *Energy Environ. Sci.*, 2025, 18, 6934-6982.
21. Y. Liu, R. Li, J. Xia, C. Shu, J. Liu, S. Yan, R. Jin, H. Chen, L. Teng, Y. Si, C. Guo, Y. Zhang and Q. Xu, *Nano Res.*, 2025, 18, 94907244.
22. X. Xie, B. Li, P. Xu, M. Sougrati, R. Garcia-Serres, D. Cullen, A. Kropf, F. Xia, M. Song, S. Saha, Y. Zeng, M. Engelhard, M. Bowden, H. Zhang, L. Yan, T. Lemmon, X. Li, U. Martinez, Y. Cheng, G. Wu, P. Zelenay, V. Ramani, D. Myers, F. Jaouen, L. Yang, G. Wang and Y. Shao, *J. Am. Chem. Soc.*, 2025, 147, 48117-48126.
23. J. Müller-Hülstede, H. Schmies, D. Schonvogel, Q. Meyer, Y. Nie, C. Zhao, P. Wagner and M. Wark, *Int. J. Hydrog. Energy*, 2024, 50, 921-930.
24. Q. Meyer, Y. Nie, M. R. Bin Mamtaz and C. Zhao, *ACS Electrochem.*, 2025, 1, 1206-1230.
25. K. Kumar, L. Dubau, F. Jaouen and F. Maillard, *Chem. Rev.*, 2023, 123, 9265-9326.
26. M. Moghaddam, M. Kafshgari, A. Bahari, L. Kafshgari and A. Jafari, *J. Energy Chem.*, 2025, 107, 305-344.
27. X. Zhao, Z. Hao, X. Zhang, L. Li, Y. Gao and L. Liu, *Chem. Eng. J.*, 2024, 497, 155005.
28. K. Jannath and H. Saputra, *Electrochem. Sci. Adv.*, 2025, 5, e202400033.
29. M. Gollasch, J. Müller-Hülstede, H. Schmies, D. Schonvogel, P. Wagner, A. Dyck and M. Wark, *Catalysts*, 2021, 11, 841.
30. B. Wang, T. Zhang, G. Wang, X. Han, X. Zheng, G. Mao and Q. Wang, *Sep. Purif. Technol.*, 2025, 356, 129934.
31. L. C. P. Pérez, N. R. Sahraie, J. Melke, P. Elsässer, D. Teschner, X. Huang, R. Kraehnert, R. J. White, S. Enthaler, P. Strasser and A. Fischer, *Adv. Funct. Mater.*, 2018, 28, 1707551.
32. Z. Jiang, X. R. Liu, X. Z. Liu, S. Huang, Y. Liu, Z. C. Yao, Y. Zhang, Q. H. Zhang, L. Gu, L. R. Zheng, L. Li, J. A. Zhang, Y. J. Fan, T. Tang, Z. B. Zhuang and J. S. Hu, *Nat. Commun.*, 2023, 14, 1822.
33. F. Luo, S. Wagner, W. Ju, M. Primbs, S. Li, H. Wang, U. I. Kramm and P. Strasser, *J. Am. Chem. Soc.*, 2022, 144, 13487-13498.
34. T. Sun, B. B. Tian, J. Lu and C. L. Su, *J. Mater. Chem. A*, 2017, 5, 18933-18950.
35. J. Piir, J. Lilloja, M. Käärik, J. Kozlova, A. Kikas, A. Treshchalov, J. Aruväli, V. Kisand, J. Leis, K. Kukli and K. Tammeveski, *Electrochim. Acta*, 2025, 527, 146226.
36. J. Lilloja, E. Kibena-Pöldsepp, A. Sarapuu, J. C. Douglin, M. Käärik, J. Kozlova, P. Paiste, A. Kikas, J. Aruväli, J. Leis, V. Sammelseg, D. R. Dekel and K. Tammeveski, *ACS Catal.*, 2021, 11, 1920-1931.
37. J. Lilloja, E. Kibena-Pöldsepp, A. Sarapuu, A. Konovalova, M. Käärik, J. Kozlova, P. Paiste, A. Kikas, A. Treshchalov, J. Aruväli, A. Zitolo, J. Leis, A. Tamm, V. Kisand, S. Holdcroft and K. Tammeveski, *ACS Appl. Energ. Mater.*, 2023, 6, 5519-5529.
38. M. Mooste, J. Müller-Hülstede, D. Schonvogel, T. Zierdt, J. Buschermöhle, K. Fuhrmann, M. Wilhelm, P. Wagner and K. A. Friedrich, *Electrochim. Acta*, 2025, 514, 145620.
39. M. Mooste, R. Kumar, S. Juvenen, J. Kozlova, A. Kikas, A. Treshchalov, M. Käärik, J. Aruväli, J. Leis, V. Kisand, K. Kukli, D. Schonvogel, P. Wagner, M. Wilhelm, K. Tammeveski and K. A. Friedrich, *Int. J. Energy Res.*, 2025, 2025, 4252866.
40. P. Moni, M. G. Pollachini, M. Wilhelm, J. Lorenz, C. Harms, M. M. Murshed and K. Rezwan, *ACS Appl. Energ. Mater.*, 2019, 2, 6078-6086.
41. P. Moni, M. Mooste, K. Tammeveski, K. Rezwan and M. Wilhelm, *RSC Adv.*, 2021, 11, 39707-39717.



42. S. Abinaya, P. Moni, V. Parthiban, A. K. Sahu and M. Wilhelm, *ChemElectroChem*, 2019, 6, 3268-3278. View Article Online
DOI: 10.1039/C9TA01012A
43. X. Wu, S. Xing, J. Luo, H. Wang, F. Huang and C. Zhao, *Energy Rev.*, 2025, 4, 100130.
44. D. Schonvogel, J. Hülstede, P. Wagner, I. Kruusenberg, K. Tammeveski, A. Dyck, C. Agert and M. Wark, *J. Electrochem. Soc.*, 2017, 164, F995-F1004.
45. J. Yang, P. Ganesan, A. Ishihara and N. Nakashima, *CHEMCATCHEM*, 2019, 11, 5929-5944.
46. J. Müller-Hülstede, D. Schonvogel, H. Schmies, P. Wagner, A. Dyck and M. Wark, *ACS Appl. Energy Mater.*, 2021, 4, 6912-6922.
47. J. Hülstede, D. Schonvogel, H. Schmies, P. Wagner, F. Schröter, A. Dyck and M. Wark, *Materials*, 2021, 14, 45.
48. J. G. Buschermöhle, J. Müller-Hülstede, H. Schmies, D. Schonvogel, T. Zierdt, R. Lucka, F. Renz, P. Wagner and M. Wark, *ACS Catal.*, 2025, 15, 4477-4488.
49. A. Dobrzanska-Danikiewicz, W. Wolany, D. Lukowiec, K. Jurkiewicz and P. Niedzialkowski, *Nanomater. Nanotechnol.*, 2017, 7, 1847980417707173.
50. V. Eswaraiyah, V. Sankaranarayanan and S. Ramaprabhu, *Nanoscale Res. Lett.*, 2011, 6, 137.
51. Z. Li, L. Deng, I. Kinloch and R. Young, *Prog. Mater. Sci.*, 2023, 135, 101089.
52. L. Ma, R. Wang, Y. H. Li, X. F. Liu, Q. Q. Zhang, X. Y. Dong and S. Q. Zang, *J. Mater. Chem. A*, 2018, 6, 24071-24077.
53. W. J. Fan, Z. L. Li, C. H. You, X. Zong, X. L. Tian, S. Miao, T. Shu, C. Li and S. J. Liao, *Nano Energy*, 2017, 37, 187-194.
54. H. Nguyen, J. Lee, E. Kwon, G. Lisak, B. Thanh, F. Ghanbari and K. Lin, *Chemosphere*, 2021, 279, 130569.
55. D. Sayfiddinov, R. Kumar, V. Sakthivel, A. Kim, S. Kim, J. Hyun and D. Yoo, *ACS Mater. Lett.*, 2026, 8, 161-170.
56. D. Sayfiddinov, R. Kumar, V. Sakthivel, S. Tamilarasi, A. Kim and D. Yoo, *J. Power Sources*, 2025, 652, 237595.
57. R. Zhang, W. Guo, M. Wu, Z. Meng and H. Tang, *Energy Fuels*, 2025, 39, 5956-5964.
58. A. Sokka, M. Mooste, M. Käärrik, V. Gudkova, J. Kozlova, A. Kikas, V. Kisand, A. Treshchalov, A. Tamm, P. Paiste, J. Aruväli, J. Leis, A. Krumme, S. Holdcroft, S. Cavaliere, F. Jaouen and K. Tammeveski, *Int. J. Hydrog. Energy*, 2021, 46, 31275-31287.
59. C. L. Li, M. C. Wu and R. Liu, *Appl. Catal. B-Environ.*, 2019, 244, 150-158.
60. S. Tian, S. Wu, J. Yang, J. Li, C. Liu, J. Shi, X. Xiang, L. Wang, Y. Sun and Q. Yang, *J. Electroanal. Chem.*, 2025, 980, 118991.
61. H. Zhong, J. Wang, Y. Zhang, W. Xu, W. Xing, D. Xu, Y. Zhang and X. Zhang, *Angew. Chem.-Int. Edit.*, 2014, 53, 14235-14239.
62. Q. Wang, T. Ina, W. Chen, L. Shang, F. Sun, S. Wei, D. Sun-Waterhouse, S. Telfer, T. Zhang and G. Waterhouse, *Sci. Bull.*, 2020, 65, 1743-1751.
63. A. Racz and M. Menyhard, *Appl. Surf. Sci. Adv.*, 2025, 30, 100872.
64. J. C. Lascovich, R. Giorgi and S. Scaglione, *Appl. Surf. Sci.*, 1991, 47, 17-21.
65. S. Turgeon and R. W. Paynter, *Thin Solid Films*, 2001, 394, 43-47.
66. T. Canuto de Almeida e Silva, M. Mooste, E. Kibena-Pöldsepp, L. Matisen, M. Merisalu, M. Kook, V. Sammelseig, K. Tammeveski, M. Wilhelm and K. Rezwani, *Catal. Sci. Technol.*, 2019, 9, 854-866.
67. R. Kumar, M. Mooste, I. Zekker, M. Käärrik, J. Leis, A. Kikas, A. Treshchalov, J. Kozlova, M. Otsus, J. Aruväli, V. Kisand, K. Kukli and K. Tammeveski, *Int. J. Hydrog. Energy*, 2025, 98, 793-806.
68. X. Zhang, S. Wang, Z. Sun, Z. Ma, H. Wang, Z. Yang, Q. Chang and W. Chen, *Nano Res.*, 2025, 18, 94907235.
69. R. Kumar, M. Mooste, Z. Ahmed, I. Zekker, M. Käärrik, M. Marandi, J. Leis, A. Kikas, M. Otsus, A. Treshchalov, J. Aruväli, M. Jaagura, V. Kisand, A. Tamm and K. Tammeveski, *J. Environ. Chem. Eng.*, 2024, 12, 112242.



70. E. Eren, N. Özkan and Y. Devrim, *Int. J. Hydrog. Energy*, 2020, 45, 33957-33967. View Article Online
DOI: 10.1039/D6TA01012A
71. Y. Jing, Y. Cheng, L. Wang, Y. Liu, B. Yu and C. Yang, *Chem. Eng. J.*, 2020, 397, 125539.
72. M. Mooste, Z. Ahmed, P. Kapitulskis, R. Ivanov, A. Treshchalov, H.-M. Piirsoo, A. Kikas, V. Kisand, K. Kukli, I. Hussainova and K. Tammeveski, *Appl. Surf. Sci.*, 2024, 660, 160024.
73. L. Li, N. Li, J. Xia, S. Zhou, X. Qian, F. Yin, G. He and H. Chen, *J. Mater. Chem. A*, 2023, 11, 2291-2301.
74. J. Lee and W. Jung, *Mol. Catal.*, 2025, 580, 115107.
75. S. Dongre, G. Zuccante, M. Muhyuddin, C. Vecchio, V. Baglio, E. Berretti, A. Lavacchi, R. Shwetharani, R. Balakrishna and C. Santoro, *Electrochim. Acta*, 2025, 517, 145763.
76. F. Ibrahim, K. Kisand, J. Douglin, A. Sarapuu, A. Kikas, M. Kaarik, J. Kozlova, J. Aruväli, A. Treshchalov, J. Leis, V. Kisand, K. Kukli, K. Yassin, D. Dekel and K. Tammeveski, *Chem. Eng. J.*, 2025, 510, 161560.
77. R. Hao, S. Gu, J. Hu, J. J. Chen, Q. M. Gan, Y. Z. Li, Z. Q. Wang, G. Y. Liu, C. L. Yan, H. M. Yuan, K. Y. Liu, C. Liu and Z. G. Lu, *Carbon*, 2023, 209, 118031.
78. T. Zierdt, T. Reuter, J. Müller-Hülstede, J. Buschermöhle, D. Schonvogel, J. Kröner, M. Schwan, B. Milow, P. Wagner and K. Friedrich, *ChemSusChem*, 2025, 18, e202401843.
79. V. Ficca, C. Santoro, E. Placidi, F. Arciprete, A. Serov, P. Atanassov and B. Mecheri, *ACS Catal.*, 2023, 13, 2162-2175.
80. Z. Cui and X. Bai, *ACS Appl. Mater. Interfaces*, 2022, 14, 9024-9035.
81. M. E. M. Buan, A. Cognigni, J. C. Walmsley, N. Muthuswamy and M. Ronning, *Catal. Today*, 2020, 357, 248-258.
82. K. X. Liu, S. Kattel, V. Mao and G. F. Wang, *J. Phys. Chem. C*, 2016, 120, 1586-1596.
83. W. J. Jiang, L. Gu, L. Li, Y. Zhang, X. Zhang, L. J. Zhang, J. Q. Wang, J. S. Hu, Z. D. Wei and L. J. Wan, *J. Am. Chem. Soc.*, 2016, 138, 3570-3578.
84. J. H. Zagal and M. T. M. Koper, *Angew. Chem.-Int. Edit.*, 2016, 55, 14510-14521.
85. Y. Hu, J. O. Jensen, C. Pan, L. N. Cleemann, I. Shypunov and Q. F. Li, *Appl. Catal. B-Environ.*, 2018, 234, 357-364.
86. Q. Z. Shu, S. X. Yang, X. Y. Zhang, Z. X. Li, Y. Zhang, Y. Tang, H. Gao, C. X. Xia, M. M. Zhao, X. F. Li and H. Zhao, *Int. J. Hydrog. Energy*, 2024, 57, 90-99.
87. T. Zierdt, M. Bin Mamtaz, T. Eek, J. Müller-Hülstede, S. Rehse, Q. Meyer, D. Schonvogel, P. Wagner, C. Zhao, M. Wark and K. Friedrich, *ChemSusChem*, 2025, 18, e202500905.
88. G. Bae, M. Kim, M. Han, J. Cho, D. Kim, M. Sougrati, J. Kim, K. Lee, S. Joo, W. Goddard, H. Oh, H. Kim, F. Jaouen and C. Choi, *Nat. Catal.*, 2023, 6, 1140-1150.
89. T. Zierdt, J. Müller-Hülstede, H. Schmies, D. Schonvogel, P. Wagner and K. A. Friedrich, *ChemElectroChem*, 2024, 11, e202300583.
90. J. Müller-Hülstede, T. Zierdt, H. Schmies, D. Schonvogel, Q. Meyer, C. Zhao, P. Wagner and M. Wark, *J. Power Sources*, 2022, 537, 231529.
91. Y. Cheng, M. E. Wang, S. F. Lu, C. J. Tang, X. Wu, J. P. Veder, B. Johannessen, L. Thomsen, J. Zhang, S. Z. Yang, S. Y. Wang and S. P. Jiang, *Appl. Catal. B-Environ.*, 2021, 284, 119717.



Data for this article will be made available at DataDOI repository at <https://datadoi.ee/> after the acceptance of the manuscript for publication.

